NANO · MICRO small
www.small-journal.com

Nanostructured Silicon Matrix for Materials Engineering

*Poting Liu, Alexander Schleusener, Gabriel Zieger, Arne Bochmann, Matthijs A. van Spronsen, and Vladimir Sivakov**

Tin-containing layers with different degrees of oxidation are uniformly distributed along the length of silicon nanowires formed by a top-down method by applying metalorganic chemical vapor deposition. The electronic and atomic structure of the obtained layers is investigated by applying nondestructive surface-sensitive X-ray absorption near edge spectroscopy using synchrotron radiation. The results demonstrated, for the first time, a distribution effect of the tin-containing phases in the nanostructured silicon matrix compared to the results obtained for planar structures at the same deposition temperatures. The amount and distribution of tin-containing phases can be effectively varied and controlled by adjusting the geometric parameters (pore diameter and length) of the initial matrix of nanostructured silicon. Due to the occurrence of intense interactions between precursor molecules and decomposition by-products in the nanocapillary, as a consequence of random thermal motion of molecules in the nanocapillary, which leads to additional kinetic energy and formation of reducing agents, resulting in effective reduction of tin-based compounds to a metallic tin state for molecules with the highest penetration depth in the nanostructured silicon matrix. This effect will enable clear control of the phase distributions of functional materials in 3D matrices for a wide range of applications.

1. Introduction

Top-down produced silicon nanowires (SiNWs) are prospective nanostructured surfaces that show highly intense visible (red) light emission at room temperature[1,2] and different vibrational and electronic properties.[3–6] In general, 1D nanostructures attract substantial research attention because they can be used as potential carriers of active nanomaterials at the intersection with other functional materials.[2,7–8] SiNW templates could play an important role in the development of novel semiconductor devices. The precise control of the morphology of semiconducting oxides at the nanometer scale is consequently of fundamental importance and, given the industrial and commercial demands, requires reproducible low-cost synthetic methods that can be implemented on an industrial scale. Toward this objective, SiNW arrays can be covered with functional oxides, such as tin oxide, e.g., via metal-organic chemical vapor deposition (MOCVD).

Sn(0) and its oxidation states, typically Sn(II) and Sn(IV), are very important functional materials that are widely applied in different areas.[9–12] For example, Sn(II) oxide is a promising p-type oxide semiconductor due to its high hole mobility.[13] It has been explored for use as a catalyst,[14] anode material,[15] coating substance,[16] and gas sensor.[17] SnO_2, which is widely known as a wide bandgap n-type semiconductor, can be applied in solar cells,[18] transparent electrodes,[19] and thin-film transistors.[20] To grow SnO_x layers on various substrates, the most widely used methods include spray pyrolysis,[21] sputtering,[22] laser ablation,[23] atomic layer deposition,[18] and chemical vapor deposition.[24] Furthermore, although Sn and its oxides have been widely studied, the evaluation of low-dimensional tin oxide nanostructures remains to be completed, which is important for obtaining specific optical and electrical properties for the desired applications.

In addition, tin(IV) tert-butoxide has been preliminarily studied, and it has been found to be an excellent precursor for the deposition of SnO_2 by MOCVD at low temperatures (200–400 °C) in the absence of an added oxidant (oxygen-containing agent, such as air or ozone).[25] Approximately 20 years ago, the same tin-based metalorganic precursor was employed to deposit uniform tin oxide nanowires at 750 °C (and up to 900 °C) with gold as the catalyst, as reported by Mathur's

P. Liu, A. Schleusener, G. Zieger, V. Sivakov
Leibniz Institute of Photonic Technology
Albert-Einstein Str. 9, 07745 Jena, Germany
E-mail: vladimir.sivakov@leibniz-ipht.de
P. Liu, A. Schleusener
Friedrich Schiller University Jena
Helmholtzweg 4, 07743 Jena, Germany
A. Schleusener
Istituto Italiano di Tecnologia
Via Morego 30, Genova 16163, Italy
A. Bochmann
Ernst Abbe University of Applied Science
Carl-Zeiss-Promenade 2, 07745 Jena, Germany
M. A. van Spronsen
Diamond Light Source Ltd.
Didcot, Oxfordshire OX11 0DE, UK
The ORCID identification number(s) for the author(s) of this article can be found under https://doi.org/10.1002/smll.202206318.

DOI: 10.1002/smll.202206318

group.[24] Furthermore, they found that SnO_2 layers deposited on Al substrates can have other phases of Sn, such as SnO and Sn_2O_3, by additional (ex situ) short-term plasma treatment.[26] However, the deposition of metallic tin phases using tin(IV) tert-butoxide as a precursor on planar or nanostructured silicon surfaces over a broad temperature range has still not been reported or discussed. From this point of view, the analysis of tin-based nanostructure growth dynamics is of high interest for further materials engineering applications.

To the best of our knowledge, this paper is the first to report the phase-selective deposition of $Sn/SnO/SnO_2$ by employing SiNWs as deposition matrices. By controlling the porosity of SiNWs and the deposition temperatures, it is possible to vary the spatial distributions of different tin oxide phases. The main reason for this phenomenon is identified in this paper, and detailed morphological and microstructural studies are conducted using surface-sensitive and destructive/nondestructive surface analytical methods. Our discovery opens a potential new route for selectively depositing different phases of functional metal oxides by employing a SiNW matrix and can further promote the development of optical-, electronic-, and biophotonic-related devices.

2. Results and Discussion

2.1. Surface Morphology and Microstructure

Morphological analysis of the deposits was performed by electron microscopy. As presented in **Figure 1**a, when SnO_2 was deposited at 600 °C on a planar silicon substrate, "rice-seed"-shaped crystals were homogeneously distributed on the whole surface. This was consistent with previous reports, suggesting a uniform deposition of crystalline SnO_2,[27] which was further confirmed by XRD studies. Under the same deposition conditions, the precursor was exposed to the top-down formed nanostructured silicon matrix. As shown in Figure 1b, the matrix contained SiNWs of ≈100 nm in diameter and 10 µm in length. Unlike the planar silicon surface, onto which the deposition was homogeneous, the surfaces of the SiNWs were covered with crystals of different sizes and shapes. Magnified SEM images of the same cross-section are shown in Figure 1d–f. Three main regions were identified. First, the upper region of the SiNWs was homogeneously covered with a smooth layer containing "rice-seed" shape features (cf. Figure 1d). These crystals were similar to what was deposited on the planar silicon surface. The middle region consisted of large crystals with a diameter of ≈300 nm (Figure 1e). Unlike the uniform distribution in the upper region, these crystals were randomly oriented along the middle region of the SiNWs. From the bottom up to ≈2.5 µm, the lower region showed a different morphology. As shown in Figure 1f, small spherical nanoparticles (NPs) were found along the SiNWs. These NPs had a diameter of ≈50 nm and were distributed quite homogeneously along the SiNWs. To identify the crystallographic phases in the realized deposits, XRD measurements were performed, as shown in Figure 1c. Furthermore, Figure 1c (black line) shows the XRD pattern of the as-deposited SnO_2 layers on the planar surface. The obtained characteristic reflexes were assigned to the tetragonal (cassiterite) Sn(IV) oxide phase. These results indicated that the precursor decomposed completely on the planar silicon surface and that crystalline SnO_2 was obtained at 600 °C. In comparison with planar silicon, more intense diffraction reflexes were obtained for the deposits on nanostructured surfaces, which were assigned to crystalline cassiterite SnO_2, tetragonal SnO, and tetragonal metallic β-tin, indicating the formation of different phases along the SiNWs.

2.2. Phase Localization

To determine the positions of the individual phases along the vertical axes of the SiNWs, which were already partially assumed from the cross-sectional SEM images, EBSD investigations were carried out along the SiNWs. FIB cutting, as shown in **Figure 2**a, was performed at 30 keV, followed by a 5 keV polishing step using gallium ions based on the approach presented in the methodology section. Due to the morphologies of the structures and the geometry required for the EBSD measurements, the EBSD investigations on these structures were very challenging to interpret. Figure 2b shows the quality map of the structures. The bright areas are areas where the band detection quality (intensity of the *Kikuchi* lines or quality of the diffraction pattern) was higher compared to the other areas. The entire length of the structures could not be identified. As a result of the 70° position, in combination with a high acceleration voltage of 30 keV, the primary electrons penetrated relatively deeply into the material. Due to their high energy and thin structures, the primary electrons migrated through the material without a backscattering process. Due to the 70° geometry, this transmission mainly occurred in the upper area of the structures. Furthermore, the backscattered electrons that satisfied the *Bragg* condition could be reabsorbed due to the irregular arrangement of the structures. An absorption or shadowing process was probably also responsible for the detection of no or only very weak signals from the lower areas of the gaps. Backscattered electrons that escaped from this area may have been reabsorbed by the sidewalls of the structures. Nevertheless, as shown in Figure 2c, we found that in the lower region, metallic Sn was the main detected phase, which is presented as a red region, reflecting the round NPs shown in Figure 1f. Moreover, the middle part, which is represented as a yellow region, was identified as Sn(II) oxide. On the top, due to the low EBSD signal, it was difficult to observe the presence of SnO_2. Therefore, the EBSD results confirm the results from the SEM and XRD measurements presented in Figure 1.

The EBSD results are based on sections obtained by focused ion etching using an ion energy of 30 keV, which is a destructive technique, as the ion impact predisposes the samples to changes in their initial chemical structures. As a consequence, to avoid possible chemical changes in the initial structures of the deposited tin-based layers, nondestructive surface-sensitive methods were used to study the electronic and atomic structures of the obtained layers on the surface and in the depth of the porous silicon matrix by applying a mechanical surface treatment using a previously published protocol.[28]

To compensate for the deficiencies of EBSD and more accurately identify the phase composition, XANES was employed.

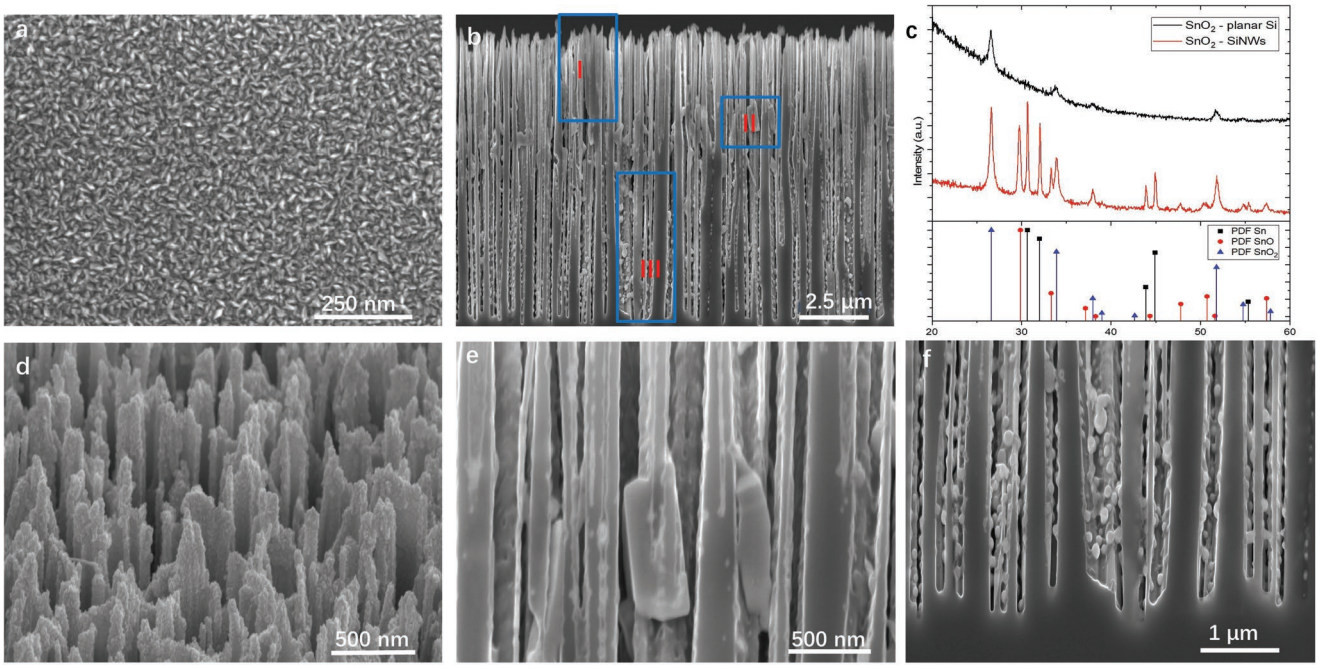

Figure 1. MOCVD-grown tin oxide layers on planar and nanostructured silicon surfaces at 600 °C. a) SEM top view of tin oxide layers grown on a planar silicon surface; b) SEM cross-sectional view of tin oxide layers grown on SiNWs; c) XRD patterns of tin oxide deposits on planar and nanostructured silicon surfaces; d) detailed SEM cross-sectional (or tilted) views of the upper (I); e) middle (II) and f) lower (III) regions of tin-based layers grown on SiNWs at 600 °C.

The O K-edge and Sn $M_{4,5}$-edge XANES spectra from the SnO_{2-x}-SiNW surface are shown in **Figure 3**. The overall intensity and background were possibly affected by the overlap from the O K-edge absorption edge and the Sn $M_{4,5}$-edge. Nevertheless, the spectra above 530 eV were assigned to oxygen contributions. According to the dipole selection rule, the XANES spectra of the O K-edge originated from O-1s transitions to O-2p states. In general, the presented spectra were divided into two regions. As shown in Figure 3a, the two low-energy peaks at ≈532 and 538 eV (Zones I and II) were assigned to the transitions into O-2p hybridized with the Sn-5s and Sn-5p states, respectively. For SnO_2, the peak at 538 eV was attributed to a further splitting process in the SnO_6 polyhedra, as reported by Gago et al.[29] Another hybridization of O-2p and Sn5d/4f states was reflected by a higher energy band (550–670 eV). In the Sn M4,5-edge XANES spectra, there are two regions related to the spin-orbit splitting of the 3d states into $3d_{5/2}$ (M5) and $3d_{3/2}$ (M4) bands. These states are distributed at different energy ranges of the spectra with an energy difference of ≈8.4 eV. According to the dipole selection rule, the Sn M4,5-edge XANES spectrum shows the transition from the Sn-3d state to the state with p and f characteristics, so it mainly maps the contribution to the empty Sn-5p conduction band and the Sn-5f orbitals. Therefore, the Sn M4,5-edge can provide clear information about the Sn oxidation state because the absorption onset changes to higher energies with increasing valence number. As a result, Sn, SnO(II), and SnO_2(IV) will have increasing energy positions on the Sn M4,5-edge XANES spectrum.

As shown in Figure 3b, the Sn M4,5-edge XANES spectra of pristine SnO_2 and the SnO_2-SiNW upper surface show the same characteristic peaks, which reflects that they have similar atomic and electronic structures, in good correlation with the detected XANES O K-edge spectra. However, in the SnO_2-SiNW lower region, shown in Figure 3b, it is clear that the intensity of the characteristic SnO_2 peaks (Zones IV and V) is reduced. Furthermore, two more peaks at lower energies of ≈486.5 and 487.0 eV are shown (Zone III), which were assigned to lower oxidation states, namely, metallic Sn(0) and Sn(II), respectively.

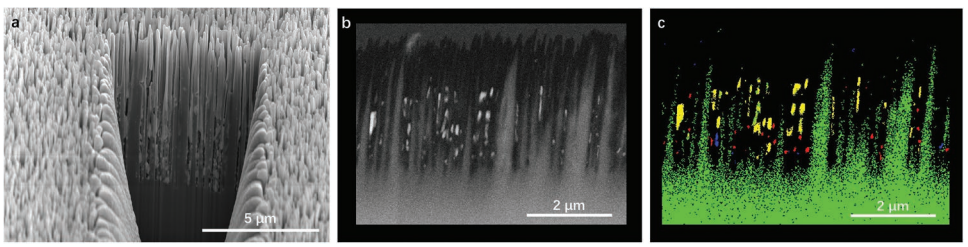

Figure 2. EBSD study of tin-based deposits on nanostructured silicon surfaces. a) SEM image of an FIB cut; b) quality map image; c) EBSD phase map for three tin phases, namely, Si (green), SnO_2 (blue), and SnO (yellow), and metallic Sn (red).

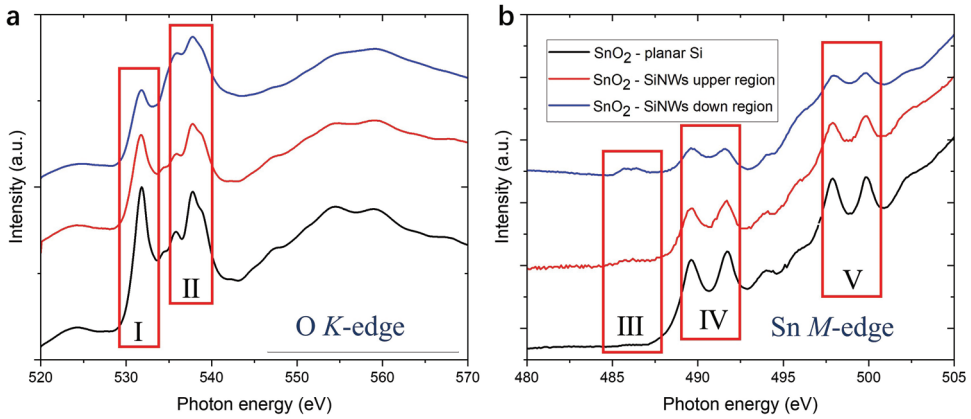

Figure 3. XANES spectra of the SnO_2-planar silicon and SnO_2-SiNW upper and lower regions. a) O K edge; b) Sn M-edge.

Notably, the Sn(II) feature at ≈487 eV was a result of the formation of oxygen vacancies in the electronic structure of SnO_2, as reported previously.[30,31] The formation of oxygen deficiencies in the SnO_2 structure changed the local surroundings of oxygen to Sn atoms, approaching SnO (through SnO_{2-x}, where $x < 2$). As a result, the electronic density of states of the Sn atoms was reconstructed in the same direction, as discussed in our previous publication.[32] In summary, in the observed O K-edge XANES spectra of all three surfaces under investigation, it is clear that the characteristic peak located at 531 eV was suppressed from the upper to the lower region in the deposit on the nanostructured surface in comparison to the planar surface, suggesting that less oxygen was present as SnO_2 on the surface, further confirming that the state distribution of tin along the SiNWs changed from SnO_2 to SnO and to metallic Sn from top to bottom along the SiNWs.

2.3. Mechanism of Phase Evolution

The observed distribution of the Sn-based phase along the vertical axes of the SiNWs can be explained by differences in the thermal conductivity of the silicon nanowires layer and bulk silicon, as well as by the irregular thermal motion of tin-based precursor molecules in the nanocapillary (the volume between nanowires can be described as nanocapillary) and the presence of alkenes (butene in our case) as reducing agent. Previously, it was reported that when a bulk silicon substrate was structured to SiNWs by applying the same top-down method applied in the present work, the thermal conductivity was reduced dramatically.[33,34] Specifically, Hochbaum et al.[34] reported that bulky silicon wafers showed a thermal conductivity of 150 W m^{-1} K^{-1}, but after the wet chemical etching process, the obtained SiNWs showed significantly reduced values below 1 W m^{-1} K^{-1}. This large difference in the thermal conductivity values between bulk Si and the SiNWs may have caused tremendous changes (in temperature distribution) on the surface during the MOCVD process. As shown in **Figure 4**a, when the substrate was heated in the MOCVD process, due to the low thermal conductivity, the heat from the bulk part (wafer) could not be efficiently transported through the SiNWs, which resulted in a temperature gradient along the SiNWs. It increased while the thermal conductivity ratio of the SiNWs and bulk Si was reduced. However, this gradient was not strong enough to explain the observed effects, according to the theoretical calculations presented in Figure 4b. According to these simulation results, a maximum temperature gradient of 10 K along SiNWs can be achieved in 10 µm matrix SiNWs.

However, irregular and chaotic thermal motion (similar to Brownian motion) of molecules in the nanocapillaries and their interaction with capillary sidewalls might lead to chemical bond destruction in the tin-based layers. The extreme aspect ratio of these capillaries resulted in the molecules experiencing a greatly increasing number of interactions with the sidewalls of the SiNWs with increasing penetration depth. This led to their advancing decomposition with respect to depth, as presented in **Figure 5**a. On the other hand, tin(IV) tert-butoxide molecular precursor decomposition byproducts are known to be butene and butanol, as was previously published by Mathur, Sivakov, et al.[35] Additionally, An et al. presented a theoretical prediction of alkene-based tin dioxide reduction.[36] Alkenes (butene in our case as a byproduct of the decomposition of the molecular tin precursor) can generate hydrogen from its decomposition as a function of surface temperature. In our case, this means that in a spatially confined nanocapillary, butene, which is much deeper penetrated in the silicon nanowires matrix, can effectively decompose, releasing hydrogen, which can act as a reducing agent for tin oxide reduction, due to the spatially confined nature of nanocapillary, so decomposition can occur at lower temperatures compared to planar structures requiring higher surface temperatures. To confirm this hypothesis, we performed depositions on planar silicon substrates at 600 and 725 °C. SEM studies showed that the surface morphology of the deposit at 600 °C is comparable to the morphology of the top surface part (cf. Figure 1d) of nanostructured silicon coated with a tin-containing coating at 600 °C, as presented in Figure 5c. The globular morphology in the deposits on planar surfaces at 725 °C, as shown in Figure 5d, corresponded to the lower surface part of nanostructured (cf. Figure 1f) silicon coated with a tin-containing coating at 600 °C. Figure 5b shows XRD patterns of deposits on planar silicon wafers at 600 and 725 °C. XRD studies show the presence of pure tin dioxide phase and a mixture of metallic and tin oxide phases in the deposits on the planar surface at 600 and 725 °C, respectively.

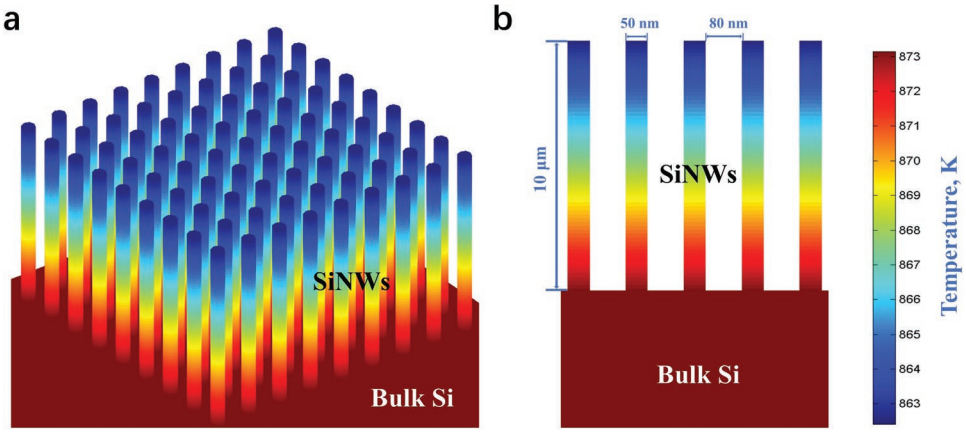

Figure 4. Theoretical simulation of thermal radiation losses during tin oxide formation on a nanostructured silicon surface. a) Aerial view; b) cross-sectional view.

These results show that the morphology that we can achieve on nanostructured silicon surfaces at 600 °C (cf. Figure 1b) can only be realized on planar silicon surfaces at temperatures of at least 125 K above. In addition, Shen et al.[37] presented that the interaction between molecules (precursor and byproducts molecules) and the nanochannels can increase the local concentration of the reactants and also enhance reaction pressure.[38] On the contrary, when the size (diameter) of nanocapillary increases, the interactions between the molecules and nanocapillary gradually weaken.[39] By varying the geometry of the initial matrix of nanostructured silicon (short and long nanocapillary), it was possible to control the presence of one or the other phase. In our previous works, we showed the flexibility of the MAWCE method for obtaining nanostructured surfaces.[40] **Figure 6** shows the results of the deposition of tin-containing films onto matrices of nanostructured silicon with different initial nanocapillary length. This geometry-based explanation is supported by the finding that an increased length of initial SiNWs enhanced the observed effect. According to the results of the XRD analysis and SEM studies, on surfaces with a shorter and longer nanocapillary length, a significantly increased amount of the metallic tin phase (as shown in Figure 6a,c for 10 min etched surface, "long") was observed in comparison with surfaces with a shorter nanocapillary length

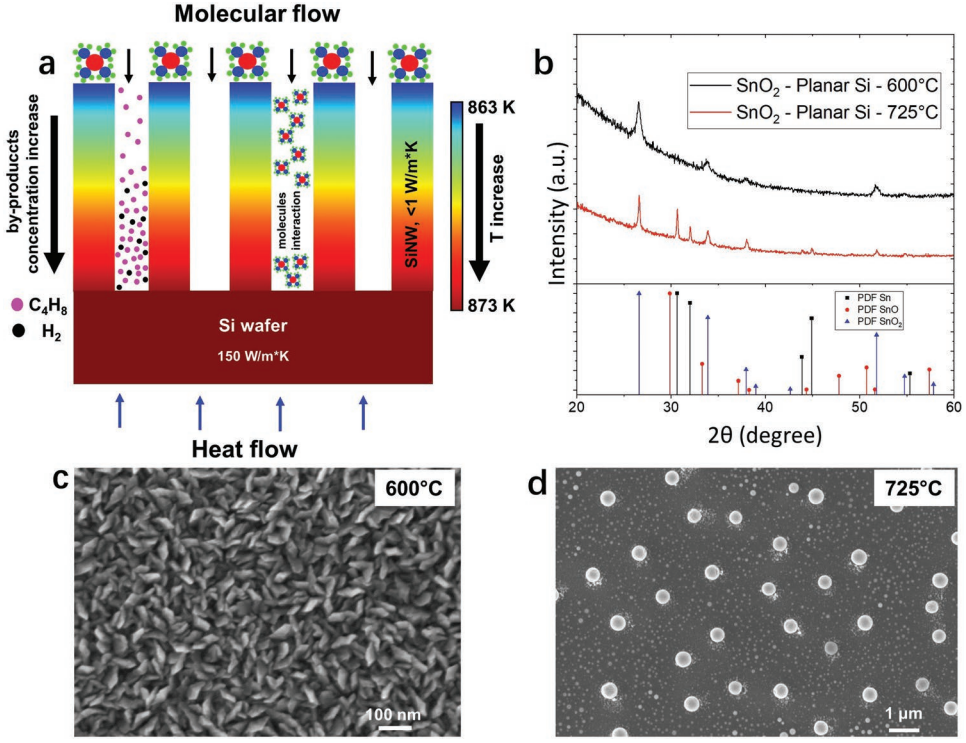

Figure 5. A possible mechanism of the phase separation along the SiNWs length. a) Schematic illustration of the proposed mechanism; b) XRD patterns of deposits on planar silicon surfaces at 600 and 725 °C, respectively; c) SEM image of SnO_2 deposited on a planar Si wafer at 600 °C; d) SEM image of SnO_2 deposited on a planar Si wafer at 725 °C.

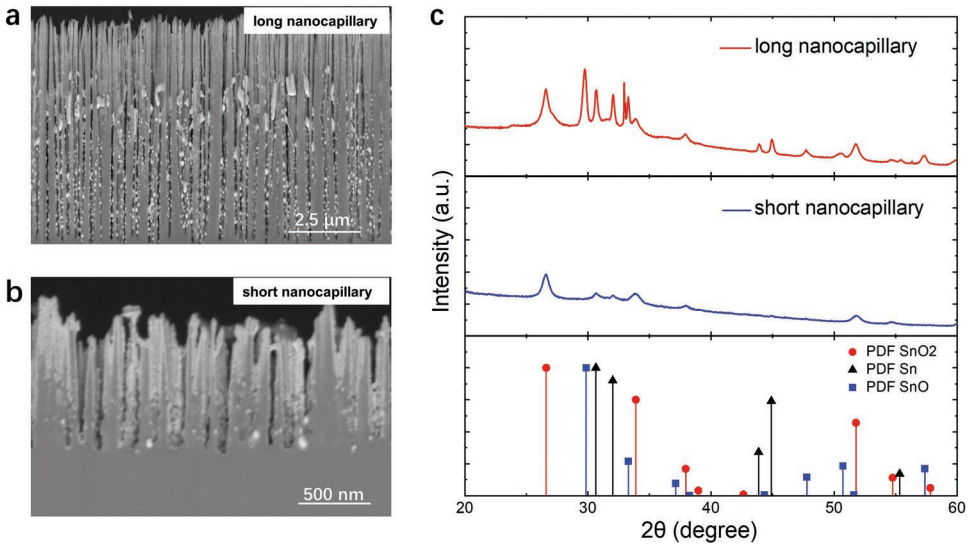

Figure 6. Phase variation by adjusting the initial nanostructured silicon matrix parameters. a) Cross-sectional SEM image of 10 min etched SiNWs matrix (long) covered with tin oxides; b) cross-sectional SEM image of 1 min etched SiNWs matrix (short) covered with tin oxides; c) XRD patterns of observed SnO_2-SiNW deposits on 10 and 1 min etched SiNWs matrices, respectively. All depositions were performed at 600 °C.

(as shown in Figure 6b,d for 1 min etched surface). This means that the geometry of the nanocapillary had the dominant effect and significantly influenced the amount of precursor molecule collisions and concentration of by-products, which could be used to reduce the tin-based molecular precursor down to the metallic state.

Our observed results clearly show that the use of a porous silicon matrix enables the realization of low-valence tin structures at lower temperatures, which makes it possible to reduce the energy consumption in the deposition of thin films. We found that even at a maximum temperature of 600 °C, it was possible to realize layers comparable to those on planar structures, but at 125 K lower temperature. In addition, it was found to be possible to create reduction gradients equivalent to a temperature difference of 125 K on a bulk material with a structure with a temperature gradient of 10 K and less along the length of the silicon nanowires. Our results additionally prove the hypothesis of the distribution of various tin-containing phases in nanostructured silicon matrices due to precursor and byproducts (butene) molecules interactions inside the nanocapillaries as a consequence of random thermal motion of the precursor molecules in nanochannel. In summary, the observed effect can be explained as an effect of geometry (silicon nanowires length) and formation of by-products, which can play a role of reducing agent, followed by enhanced movement of precursor molecules in the nanocapillary and their interaction inside the nanocapillary (with other molecules, sidewalls, and by-products), which leads to a localized reduction of tin oxide. These results open a new wide possibility for the application of nanostructured silicon matrices in the nanoengineering of functional materials.

3. Conclusion

In the present paper, we described a novel effect related to the phase-controlled deposition of tin-based coatings by employing top-down nanostructured silicon surfaces as deposition channels. We found that the formation of different tin-based phases along nanochannel can be explained by the presence of nanocapillaries in the initial nanostructured silicon surface, so that when molecules penetrate the porous silicon matrix, they are exposed to random thermal motion (similar to Brownian motion) inside the nanocapillaries, which leads to effective decomposition of the precursor molecule. In addition, we hypothesized that the decomposition byproducts of the molecular precursor, in our case butene, can effectively reduce tin oxide to the metallic state in the lower parts of the matrix. The upper and lower parts of a SiNW matrix covered with tin-based layers were systematically investigated by applying surface-destructive and surface-sensitive nondestructive analytical methods. Atomic and electronic structure studies of observed deposits using XANES and synchrotron radiation proved the presence of a tin-based phase distribution along the vertical axes of the SiNWs. This discovered effect opens a new and easy route to the phase-selective deposition of functional materials with lower energy consumption and further expands the application of top-down nanostructured silicon surfaces in materials engineering as an anode with high electronic conductivity for high-performance lithium-ion batteries[41] or as UV-SERS active surface for biophotonics.[42]

4. Experimental Section

SiNWs Preparation: P-type lowly doped silicon (100) wafers (boron doped, resistivity: 1–10 ohm cm) from Si-Mat GmbH, Germany, were used to prepare SiNWs using the metal-assisted wet chemical etching (MAWCE) method. Silicon wafers with dimensions of 1×1 cm^2 were cleaned by ultrasonic rinsing in acetone and isopropanol every 3 min. After that, each wafer was immersed into a 2% HF bath to remove the native oxidized layer. Then the wafer was cleaned in deionized water and dried with insert gas. The formation of SiNWs includes two steps. In the first step, silver nanoparticles were deposited on silicon wafers

using aqueous solutions initially containing 0.05 M $AgNO_3$ and 5 M HF at a 1:1 (v/v) ratio for 30 s. In the second step, silicon wafers covered with Ag nanoparticles were immersed in a second etching solution containing 5 M HF and 30% H_2O_2 at a 10:1 (v/v) ratio for 10 min at room temperature. Subsequent anisotropic etching occurred in the HF/H_2O_2 solution. Afterward, SiNW arrays were rinsed several times in deionized water and dried at room temperature. SiNW arrays were treated with a concentrated 65% nitric acid solution for 10 min to remove the AgNPs from the SiNW surfaces. After that, the samples were immersed into a 2% HF solution to remove the oxide layer that was produced during the HNO_3 and H_2O_2 treatments. Finally, the samples were washed with deionized water and dried with nitrogen at room temperature.

MOCVD Process: The MOCVD process used a volatile organometallic compound, tin(IV) tert-butoxide ($Sn(O^tBu)_4$), with an initial oxidation number of four. $Sn(O^tBu)_4$ was synthesized by a chemical process using the Schlenk line system based on a procedure reported by Chandler.[43] The purity of the synthesized precursor was determined by 1H NMR analysis.

Tin-tin oxide films were deposited using a horizontal cold wall CVD reactor. The synthesized $Sn(O^tBu)_4$ was used as a precursor for functional surface formation. Metal oxide films were deposited in a nonoxygen atmosphere (dynamic vacuum) due to the high sensitivity of the precursor molecules to atmospheric moisture at 10^{-3} Torr pressure. In the beginning, the substrate holder (graphite based) was heated to 500 °C to remove the residual organic compounds and to evaporate water from the reaction zone. After this process, the system was cooled to room temperature, and the precursor was introduced under an inert gas atmosphere. Furthermore, each silicon wafer with SiNWs was heated to the film growing temperature at 600 °C using an induction heating method; additionally, the temperature of the substrate surface was controlled using an IR thermal detector. The precursor flow was transported to the hot substrate surface by vacuum. After the deposition process for 10 min, the system was cooled and vented to obtain samples.

SEM: Electron microscopy studies to elucidate the morphologies of SnO_2 deposits on the planar and nanostructured silicon surfaces were carried out using a Helios NanoLab 600i dual-beam device from the company FEI at the Institute of for Solid State Physics at Friedrich Schiller University Jena and a field-emission Ultra55 scanning electron microscope from the Zeiss company at Ernst Abbe University of Applied Sciences in Jena.

XRD: To elucidate the crystal structure and composition, SnO_2 layers were deposited on planar and nanostructured silicon surfaces using an X'Pert Pro X-ray diffractometer from PANalytical B.V. in the Bragg-Brentano configuration.

EBSD: For a more detailed crystallographic phase investigation, EBSD measurements on gallium ion beam-prepared cross-sections of the SnO_2-coated nanostructured surfaces were performed. The investigations were carried out using a field-emission Ultra55 scanning electron microscope from the Zeiss company at Ernst Abbe University of Applied Sciences in Jena. This microscope was equipped with an EBSD detector from Bruker.

FIB Cut Preparation: A cross-section was prepared in several steps using a 52°-tilted specimen in an FEI dual-beam *Helios NanoLab 600i* system. The ion energy remained constant at 30 keV during the individual preparation steps. The first cut was made at a high ion current of 21 nA. In the subsequent steps, the ion current was gradually reduced to 80 pA. The reduction of the ion current was necessary to prevent the redeposition of the ablated material as much as possible. Since less material was removed per unit time at a low ion current (e.g., 80 pA) than at a high ion current (e.g., 21 nA), analogous to the reduction of the ion current, the length and width of the preparation area were reduced (shortening the preparation time). Due to the superposition of several collision cascades and the resulting displacement of the sample atoms from their original lattice sites, an amorphous layer formed in the area of the sample close to the surface. Since the amorphous layer could have had a disturbing effect on the subsequent EBSD measurements, the entire prepared area was polished at a reduced ion energy in a final step. For this purpose, the sample was tilted by an additional 3°–55°, and the previously prepared area was polished with an ion energy of 5 keV and an ion current of 0.12 nA.

XANES: The samples were fixed onto an aluminum sample plate using carbon tape and loaded into end station 2 of B07B,[44] where the total electron yield (via the sample drain current) was simultaneously recorded for the O-K and Sn-$M_{4,5}$ edges. The photodiode (AXUV 100G) was shielded with a 40 nm thick Al foil to block electrons and stray light. The SiN_x window separating the end station from the beamline was removed for all edges, as both the window and the sample contained Si. Spectra were recorded using a Au-coated grating with 600 lines per mm and exit slits of dimensions 1.5 mm × 0.04 mm (nondispersive and dispersive directions, respectively). All measurements were obtained at room temperature, under high vacuum (mid 10^{-8} mbar), and with the beam under normal incidence. As a reference for the photon flux, I_0, the photocurrent emitted from the final refocusing mirror was collected via an electrode opposing the mirror and biased at +36 V.

Temperature Gradient Simulations along SiNWs: A model was created using Comsol Multiphysics software,[45] which is a simplified representation of the SiNWs based on a homogeneous silicon substrate and a 9 × 9 element array of homogeneous cylinders representing the SiNWs. Due to the negligible differences between elements at the border and the center of the array, this array can also be used as a representative model for the structures of millions of SiNWs on a chip. The model was intended to describe an extreme case in the sense of thermal loss by radiation. This enabled to estimate whether the observed effect on the SiNW sidewalls could be attributed to a thermal gradient along the SiNWs. Hence, a SiNW geometry was chosen for the model that represents the highest thermal resistance expected: The observed maximum length of 10 µm was chosen as the SiNW length, while a diameter of 50 nm was chosen at the lower end of the typical range. The distance of the SiNW was again set to rather large value (80 nm). A silicon substrate of 525 µm thickness and 150 W m^{-1} K^{-1} was assumed, while for the SiNWs, a low value of 0.25 W m^{-1} K^{-1} was chosen. The radiative loss was assumed to result from the tips of the SiNWs with an emissivity of 1. The radiation from the sides of the SiNWs was considered by creating an effective surface area at each tip, which scales up the emissivity by a factor of $e = A_{sq}/A_{tip}$, where A_{tip} and A_{sq} correspond to the geometrical areas of the SiNW tip and a lateral 2D unit cell containing exactly one SiNW, respectively. Most of the radiation was found to be absorbed or reflected by the surrounding SiNWs. Thus, in the case of a maximized gradient, 100% absorption and radiative losses of an effective area equivalent to the whole plane containing the SiNW tips were assumed. The real gradient was then smaller than the resulting value because emission from the warmer parts of the SiNW closer to the substrate as well as the substrate itself heated the upper parts of the SiNW. For the extreme case estimation, the emission of the substrate was set to zero, as well as the emission from the SiNW sidewalls, as these are already compensated by the effective area described above. Using these settings, the model yields an upper limit of the thermal gradient that can occur along the SiNWs.

Acknowledgements

V.S. and P.L. gratefully acknowledge financial support by the German Research Foundation (DFG) under grant no. SI1893/27-1. V.S. is grateful to Prof. Carsten Ronning at Friedrich Schiller University and Prof. Steffen Teichert at Ernst Abbe University of Applied Sciences both in Jena/Germany for providing the SEM/FIB and EBSD facilities. P.L. and V.S. are grateful to Dr. Marco Diegel and Christa Schmidt for XRD measurements. This work was carried out with the support of Diamond Light Source, beamline B07-B (proposal cm31119-2). Dave C. Grinter and Pilar Ferrer-Escorihuela are gratefully acknowledged for their instrumental work in commissioning beamline B07B.

Open access funding enabled and organized by Projekt DEAL.

Conflict of Interest

The authors declare no conflict of interest.

Data Availability Statement

The data that support the findings of this study are available from the corresponding author upon reasonable request.

Keywords

nanocapillary, phase control, silicon nanowires, tin oxides, XANES

Received: October 14, 2022
Revised: December 20, 2022
Published online:

[1] A. Irrera, M. J. Lo Faro, C. D'Andrea, A. Alessio Leonardi, P. Artoni, B. Fazio, R. Anna Picca, N. Cioffi, S. Trusso, G. Franzò, P. Musumeci, F. Priolo, F. Iacona, *Semicond. Sci. Technol.* **2017**, *32*, 043004.
[2] V. Sivakov, F. Voigt, A. Berger, G. Bauer, S. H. Christiansen, *Phys. Rev. B* **2010**, *82*, 125446.
[3] F. Fabbri, E. Rotunno, L. Lazzarini, N. Fukata, G. Salviati, *Sci. Rep.* **2014**, *4*, 3603.
[4] J. Bandet, B. Despax, M. Caumont, *J. Phys. D Appl. Phys.* **2002**, *35*, 234.
[5] X. Xu, P. Servati, *Nano Lett.* **2009**, *9*, 1999.
[6] R. A. Minamisawa, M. J. Suess, R. Spolenak, J. Faist, C. David, J. Gobrecht, K. K. Bourdelle, H. Sigg, *Nat. Commun.* **2012**, *3*, 1096.
[7] V. Sivakov, F. Voigt, in *Nanowires – Fundamental Research* (Ed: A. Hashim), IntechOpen, Croatia **2011**, p. 3.
[8] S. Li, W. Ma, Y. Zhou, X. Chen, Y. Xiao, M. Ma, F. Wei, X. Yang, *J. Solid State Chem.* **2014**, *213*, 242.
[9] A. Tricoli, S. E. Pratsinis, *Nat. Nanotechnol.* **2010**, *5*, 54.
[10] Z. Yu, Z. Yang, Z. Ni, Y. Shao, B. Chen, Y. Lin, H. Wei, Z. J. Yu, Z. Holman, J. Huang, *Nat. Energy* **2020**, *5*, 657.
[11] B. Zhao, Z. Wan, Y. Liu, J. Xu, X. Yang, D. Shen, Z. Zhang, C. Guo, Q. Qian, J. Li, R. Wu, Z. Lin, X. Yan, B. Li, Z. Zhang, H. Ma, B. Li, X. Chen, Y. Qiao, I. Shakir, Z. Almutairi, F. Wei, Y. Zhang, X. Pan, Y. Huang, Y. Ping, X. Duan, X. Duan, *Nature* **2021**, *591*, 385.
[12] Y. Lei, Y. Li, C. Lu, Q. Yan, Y. Wu, F. Babbe, H. Gong, S. Zhang, J. Zhou, R. Wang, R. Zhang, Y. Chen, H. Tsai, Y. Gu, H. Hu, Y. H. Lo, W. Nie, T. Lee, J. Luo, K. Yang, K. I. Jang, S. Xu, *Nature* **2022**, *608*, 317.
[13] M. Minohara, A. Samizo, N. Kikuchi, K. K. Bando, Y. Yoshida, Y. Aiura, *J. Phys. Chem. C* **2019**, *124*, 1755.
[14] H. Su, Q. Zhao, Y. Wang, Q. Zhao, C. Jang, Y. Niu, W. Lou, Y. Qi, *Catal. Commun.* **2022**, *162*, 106370.
[15] J. H. Shin, J. Y. Song, *Nano Convergence* **2016**, *3*, 9.
[16] X. C. Liu, L. T. Guo, J. Q. Gao, T. W. Guo, L. Liu, S. B. Li, X. N. Li, *Key Eng. Mater.* **2008**, *368*, 1268.
[17] P. H. Suman, A. A. Felix, H. L. Tuller, J. A. Varela, M. O. Orlandi, *Sensor Actuat. B: Chem.* **2015**, *208*, 122.
[18] Y. Kuang, V. Zardetto, R. van Gils, S. Karwal, D. Koushik, M. A. Verheijen, L. E. Black, C. Weijtens, S. Veenstra, R. Andriessen, W. M. M. Kessels, M. Creatore, *ACS Appl. Mater. Interfaces* **2018**, *10*, 30367.
[19] V. Zardetto, B. L. Williams, A. Perrotta, F. Di Giacomo, M. A. Verheijen, R. Andriessen, W. M. M. Kessels, M. Creatore, *Sustainable Energy Fuels* **2017**, *1*, 30.
[20] P. D. M, R. Mannam, M. S. R. Rao, N. DasGupta, *Appl. Surf. Sci.* **2017**, *418*, 414.
[21] S. P. Choudhury, S. D. Gunjal, N. Kumari, K. D. Diwate, K. C. Mohite, A. Bhattacharjee, *Mater. Today: Proc.* **2016**, *3*, 1609.
[22] M. Ferreira, J. Loureiro, A. Nogueira, A. Rodrigues, R. Martins, I. Ferreira, *Mater. Today: Proc.* **2015**, *2*, 647.
[23] D. C. Onwudiwe, *Mater. Res. Express* **2019**, *6*, 125004.
[24] S. Mathur, S. Barth, H. Shen, J. C. Pyun, U. Werner, *Small* **2005**, *1*, 713.
[25] J. R. Brown, M. T. Cheney, P. W. Haycock, D. J. Houlton, A. C. Jones, E. W. Williams, *J. Electrochem. Soc.* **1997**, *144*, 295.
[26] S. Mathur, R. Ganesan, I. Grobelsek, H. Shen, T. Ruegamer, S. Barth, *Adv. Eng. Mater.* **2007**, *9*, 658.
[27] K. Juraic, D. Gracin, M. Culo, Z. Rapljenovic, J. R. Plaisier, A. Hodzic, Z. Siketic, L. Pavic, M. Bohac, *Materials* **2020**, *13*, 5182.
[28] S. Y. Turishchev, E. V. Parinova, A. K. Pisliaruk, D. A. Koyuda, D. Yermukhamed, T. Ming, R. Ovsyannikov, D. Smirnov, A. Makarova, V. Sivakov, *Sci. Rep.* **2019**, *9*, 8066.
[29] R. Gago, S. Prucnal, J. Azpeitia, D. Esteban-Mendoza, I. Jiménez, *J. Alloy. Compd.* **2022**, *902*, 163768.
[30] S. Kucheyev, T. Baumann, P. Sterne, Y. Wang, T. van Buuren, A. Hamza, L. Terminello, T. Willey, *Phys. Rev. B* **2005**, *72*, 035404.
[31] O. A. Chuvenkova, E. P. Domashevskaya, S. V. Ryabtsev, Y. A. Yurakov, A. E. Popov, D. A. Koyuda, D. N. Nesterov, D. E. Spirin, R. Y. Ovsyannikov, S. Y. Turishchev, *Phys. Solid State* **2015**, *57*, 153.
[32] S. Turishchev, O. Chuvenkova, E. Parinova, M. Manyakin, S. P. Kurganskii, A. D. O. Marchenko, R. P. Liu, V. Sivakov, **2023**, https://doi.org/10.1002/smll.202206322.
[33] A. I. Boukai, Y. Bunimovich, J. Tahir-Kheli, J. K. Yu, W. A. Goddard, 3rd, J. R. Heath, *Nature* **2008**, *451*, 168.
[34] A. I. Hochbaum, R. Chen, R. D. Delgado, W. Liang, E. C. Garnett, M. Najarian, A. Majumdar, P. Yang, *Nature* **2008**, *451*, 163.
[35] S. Mathur, V. Sivakov, H. Shen, S. Barth, C. Cavelius, A. Nilsson, P. Kuhn, *Thin Solid Films* **2006**, *502*, 88.
[36] H. An, M. Yoo, H. Ha, H. Choi, E. Kang, H. Y. Kim, *Sci. Rep.* **2019**, *9*, 16702.
[37] Y. Shen, X. Wang, J. Lei, S.h. Wang, Y. Hou, X. Hou, *Nanoscale Adv.* **2022**, *4*, 1517.
[38] W. A. Solomonsz, G. A. Rance, B. J. Harris, A. N. Khlobystov, *Nanoscale* **2013**, *5*, 12200.
[39] L. Jing, C. Tang, Q. Tian, T. Liu, S. Ye, P. Su, Y. Zheng, J. Liu, *ACS Appl. Mater. Interfaces* **2021**, *13*, 39763.
[40] G. Venturi, A. Castaldini, A. Schleusener, V. Sivakov, A. Cavallini, *Nanotechnology* **2015**, *26*, 195705.
[41] Z. Dong, W. Du, H. Gu, Y. Long, C. Zhang, G. Chen, Z. Feng, W. Sun, Y. Jiang, Y. Liu, Y. Yang, J. Gan, M. Gao, H. Pan, *Small Struct* **2022**, *3*, 2100174.
[42] J. M. McMahon, G. C. Schatz, S.t. K. Gray, *Phys. Chem. Chem. Phys.* **2013**, *15*, 5415.
[43] C. D. Chandler, G. D. Fallon, A. J. Koplick, B. O. West, *Aust. J. Chem.* **1987**, *40*, 1427.
[44] D. C. Grinter, F. Venturini, P. Ferrer, M. A. van Spronsen, R. Arrigo, W. Quevedo Garzon, K. Roy, A. I. Large, S. Kumar, G. Held, *Synchrotron Radiat. News* **2022**, *35*, 39.
[45] COMSOL Multiphysics® v. 6.0. www.comsol.com, COMSOL AB, Stockholm, Sweden.